Two-scale Porosity Effects on Cohesive Crack Growth in a Ductile Media

Y. Cui[1], Y. F. Gao[2], H.B. Chew[1,*]

1. Department of Aerospace Engineering, University of Illinois at Urbana-Champaign, Urbana IL 61801, USA

2. Department of Materials Science and Engineering, University of Tennessee, Knoxville, TN 37996, USA

*Author to whom all correspondence should be addressed. Email: hbchew@illinois.edu

Abstract

Microstructures with two distinct size-scales of voids are commonplace in additively-manufactured metals. The smaller-scale voids nucleate from inclusions within the metal, while the larger-scale voids originate from unsintered powder particles. In this work, we study the interaction between these two size-scales of voids ahead of a crack, and the influence on the ductile fracture process. We adopt a finite element model of a centerline crack subjected to small-scale yielding conditions. The diffuse process zone ahead of the crack is modeled by several rows of void-containing cell elements governed by a Gurson porous material relation. Results show that the larger-scale voids near the initial crack tip generally reduces the fracture toughness by facilitating void coalescence with the crack-tip to form a single contiguous damage zone. However, strategic placements of these larger-scale voids within the active plastic zone of the crack-tip can promote crack-tip shielding, leading to diffused damage in the form of multiple unconnected damage zones, and ultimately, a several-fold improvement in toughness. We quantify the fracture behavior, as a function of the relative size and proportion of larger-scale voids in the diffuse process zone, by reconstructing the equivalent crack-tip cohesive zone laws in an elasto-plastic medium via nonlinear field projection. We demonstrate that the cohesive strength, cohesive energy, as well as the functional form of the cohesive zone law, are strongly

dependent on the dual void size-scales, which introduces a size-effect into the homogenized traction-separation relationship.

Keywords: Additively-manufactured metals; void interaction; crack growth; fracture; micromechanics modeling

1. Introduction

All natural and engineering materials contain voids at some length-scales which control the mechanical properties [1,2]. Even in highly densified materials, defects in the form of voids still dominate the failure process and limit structural design. Often, materials that fail by ductile fracture contain voids of different size-scales. In metallic alloys, for example, the primary voids first nucleate from inclusions (e.g. MnS and carbide inclusions in steel) at low stress levels during early stage loading [3]. When these primary voids grow and get closer, high local stress triaxiliaty and local plastic strains develop in the ligament between these enlarged primary voids, and induce the nucleation of secondary voids to form a two-scale porosity structure. Void interaction studies show that these secondary voids experience an elevated local stress field compared to the average stress in the material, due to local zones of high stress concentration emitted by the primary voids [4-6]. Compared to the primary voids, these secondary voids have substantially higher growth rates at average stresses below the cavitation instability level [7,8]. These detailed understanding of the synergistic interactions between voids of different scales have led to more accurate micromechanical modeling of the void coalescence behavior [9,10].

The coexistence of primary and secondary voids in conventional metallic alloys occurs only during the initiation of void coalescence after significant plastic deformation. In additively-manufactured (AM) metals, however, two different size-scales of voids can coexist even prior to significant plastic deformation. Larger-scale voids (~20-40 μm in diameter) are pre-existing in

the AM metal and originate from gas entrapment or unsintered powder particles [11-16], while smaller-scale intrinsic voids (~2-12 μm in diameter) can also nucleate from the inclusions at low stress levels and are akin to those in conventional metals. To-date, the effects of these hierarchical scales of pre-existing voids on the crack path and ultimately fracture toughness are still not well established.

The micromechanical process of void growth and coalescence occurs within a process zone ahead of the crack. A widely adopted approach to link this fracture process to the macroscopic failure behavior is to model the process zone with an equivalent cohesive zone law. This constitutive law describes the relationship between cohesive-zone tractions in equilibrium with the stress fields of the surrounding body and the cohesive-zone separations compatible with the deformation fields of the surrounding body [17,18]. Ideally, the cohesive zone traction-separation relationship embodies the entire micromechanical void growth and coalescence process within the process zone, but its exact functional form, particularly in the presence of multiple interacting voids of different size-scales, is unknown. Traditionally, the functional form of the cohesive zone law (e.g. exponential, trapezoidal, bilinear, etc.) is assumed a priori, and the cohesive strength (peak traction in cohesive zone law) and cohesive energy (area bounded by cohesive zone law) are treated as the two important material parameters to describe macroscopic fracture behavior, which are calibrated against measurement data [19-22]. Studies, however, have shown that the functional form of the cohesive zone law could be indicative of the actual micromechanical failure process [23-26]. This has led to recent efforts adopting inverse methods to reconstruct the exact functional form of the cohesive zone laws governed by different micromechanical processes in both elastic and elasto-plastic materials [27-31].

The functional form of the cohesive zone law, together with the cohesive strength and energy, provides a homogenized view of the fracture process but cannot offer detailed insights into the actual failure micromechanics. Xia and Shih simplified the ductile fracture process by confining damage to a single row of void-containing computational cells ahead of the crack-tip to represent the fracture process zone [32]. This cell-element approach is capable of reproducing the details of damage dissipation, i.e. void nucleation, growth, and coalescence, within the process zone to predict monotonic or even fatigue crack growth [33-35]. Studies have also implemented discrete voids ahead of the crack, in place of computational cells, to detail with high-resolution the void interaction effects within a variety of materials [30,36-38].

In this work, we investigate the cracking patterns and void interaction mechanisms in a ductile media resembling AM metals containing two size-scales of pre-existing voids, and subjected to small-scale yielding conditions. In the presence of a non-uniform distribution of voids of different size-scales, damage becomes more diffuse and the crack path will deviate accordingly, which precludes the use of a single row of void-containing cells to represent the fracture process zone (FPZ) [10,32,38]. In Section 2, we detail the modeling of this broader diffuse FPZ ahead of the crack by implementing several rows of void-containing computational cells with random distributions of initial porosities of two distinct size-scales. This allows the (undulating) crack to propagate naturally within the inhomogeneous process zone. We also introduce an inverse nonlinear field projection method (FPM) to homogenize the damage process with an equivalent crack-tip cohesive zone law [31]. In Section 3, we quantify the relative void size and void distribution effects on the crack-tip fracture process, crack path, and cohesive behavior. We follow with a discussion in Section 4, and conclude with a summary.

2. Modeling

2.1 Boundary value problem

Our small-scale yielding model consists of a homogeneous material with a semi-infinite crack loaded remotely by mode I *K*-field loading under plane strain conditions (Fig. 1a). Outside of the FPZ, we assume an elasto-plastic background material with Young's modulus E and Poisson's ratio ν and with uniaxial tensile stress-strain behavior described by the true stress-logarithmic strain relation

$$\varepsilon = \frac{\sigma}{E}\,, \sigma < \sigma_0$$

$$\varepsilon = \frac{\sigma_0}{E}\left(\frac{\sigma}{\sigma_0}\right)^{1/N}\,, \sigma \geq \sigma_0 \tag{1}$$

where σ_0 is the initial yield stress, and N the strain hardening exponent. Generalization to multiaxial stress states assumes isotropic hardening and von Mises yield condition.

We model the porous FPZ with 17 rows of uniformly sized cell elements ahead of the initial crack-tip, each row of 117 cell elements (Fig. 1b and 1d). Each cell, the size of $D \times D$, contains a void of initial volume fraction f_0. The behavior of a cell element is governed by the Gurson flow potential [39]

$$\Phi = \left(\frac{\sigma_e}{\bar{\sigma}}\right)^2 + 2q_1 f \cosh\left(\frac{3q_2\sigma_m}{2\bar{\sigma}}\right) - (1 + (q_1 f)^2) = 0 \tag{2}$$

where σ_e denotes the macroscopic effective stress, σ_m the mean stress, $\bar{\sigma}$ an equivalent tensile flow stress representing the actual microscopic stress-state in the matrix, and f is the current void volume fraction. Parameters q_1 and q_2 were introduced by Tvergaard [40] to improve model predictions for periodic arrays of cylindrical and spherical voids, and are taken to be 1.48

and 1.013 respectively [41]. Note that (2) reduces to von Mises yield criterion when $f = 0$. The void growth rate obeys the volumetric plastic strain rate relation

$$\dot{f} = (1 - f)\ \mathrm{tr}\ \mathbf{d}^{\mathrm{p}} \tag{3}$$

with nucleation neglected. Here $\mathrm{tr}\ \mathbf{d}^{\mathrm{p}}$ implies trace of the plastic deformation rate $\mathbf{d}^{\mathrm{p}}$.

Our finite element simulations are performed using the open source 3D finite element code WARP3D. We adopt the material parameters $\frac{\sigma_0}{E} = 0.004$, $\upsilon = 0.3$, $N = 0.05$ for all simulations, which resemble the mechanical properties of Mg alloy. The porous FPZ for our two-scale porosity simulations consists of two distinct size-scales of voids. Smaller-scale voids have fixed initial porosities of $f_0 = 0.005$, and are termed as the background porosity. The percentage proportion of randomly-distributed larger-scale voids in the process zone is denoted by α; the porosity of each larger-scale void is β times larger than the smaller-scale void, i.e. $f_0 = 0.005\beta$. Thus, $\alpha = 0$ or $\beta = 1$ infers the absence of larger-scale voids, while $\alpha = 10$ infers that 10% of the total number of cell elements within the diffuse FPZ have a porosity of $f_0 = 0.005\beta$ while the remaining 90% of the cell elements have a background porosity of $f_0 = 0.005$. The void growth process is described by (2) and (3). The location of the current crack-tip is operationally defined at a porosity of $f_{\mathrm{tip}} = 0.1$. When the porosity of an element f reaches the critical void volume fraction $f_{\mathrm{c}} = 0.2$, an element extinction procedure of WARP3D is invoked to remove the cell element and to allow crack growth.

In our simulations, both the larger-scale and smaller-scale voids are modeled to be pre-existing in the AM metal. In reality, only the larger-scale voids are pre-existing, and originate from gas entrapment or unsintered powder particles [11-16] while smaller-scale intrinsic background voids nucleate from cavities of reinforcement particles. However, prior studies have

shown that the overall response of the Gurson cell does not depend on whether the void is present from the outset or nucleates later on, provided that the nucleation would occur at a stress level below the maximum stress a cell can carry with an initial void present [22,42]. Since the background voids can nucleate from inclusions at relatively low stress levels which are well below the macroscopic stress that develops ahead of the crack front, it can therefore be assumed that these background voids in the FPZ are present from the beginning.

Along the remote circular boundary (Fig. 1a), the elastic asymptotic in-plane displacement fields

$$u_1(R,\theta) = K_I \frac{1+v}{E}\sqrt{\frac{R}{2\pi}}(3-4v-\cos\theta)\cos\frac{\theta}{2}$$

$$u_2(R,\theta) = K_I \frac{1+v}{E}\sqrt{\frac{R}{2\pi}}(3-4v-\cos\theta)\sin\frac{\theta}{2} \tag{4}$$

are prescribed under plane strain conditions, where $R^2 = x_1^2 + x_2^2$ and $\theta = \tan^{-1}(x_2/x_1)$ for nodes on the remote boundary. For the crack geometry in this study, the energy release rate or *J*-integral is related to the mode I stress intensity factor K_I by

$$J = \frac{1-v^2}{E}K_I^2 \tag{5}$$

To verify that small-scale yielding condition is satisfied, we compute the *J*-integral on several contours around the crack using domain integral method at various loading stages [43]. The domain integral values were in good agreement with the value given in (5) for the prescribed value of K_I.

2.2 Nonlinear field projection method (FPM)

As aforementioned, cohesive zone laws provide a homogenized view of the crack-tip fracture processes. One promising method to identify the crack-tip cohesive zone relations from elastic far-fields is the inverse solution developed by Hong and Kim [44], which utilizes the path-independent interaction *J*-integral applied to an eigenfunction expansion of a cohesive crack-tip field in an isotropic, homogeneous elastic solid. This field projection method (FPM) provides a systematic way of uncovering the shape of the cohesive zone laws governed by different micromechanical fracture processes. Several different forms of the FPM have been developed [27-30,45-48], with some utilizing the principle of virtual work in place of interaction *J*-integrals [45-48].

While the FPM is applicable to linear elastic materials, the plastic zone size will be considerably larger in the presence of a diffuse process zone with two size-scales of voids. This plastic dissipation contributes to the much higher steady-state versus fracture initiation toughness. In order to capture the cohesive zone law associated with cracking initiation rather than steady-state crack growth, i.e. one where the cohesive zone law does not explicitly include the contribution of the background plastic dissipation, we adopt a nonlinear FPM to reconstruct the equivalent cohesive zone law in an elasto-plastic medium [31]. Specifically, the approach inversely reconstructs the equivalent *unknown* tractions along ∂R_1 centered about $x_2 = 0$ (solid lines, Fig. 1b), from the *known* stress and displacement fields $S[\sigma_{ij}, u_j]$ along ∂R_2 (dashed lines, Fig. 1b) taken within the elasto-plastic region surrounding the process zone. The approach utilizes the Maxwell-Betti reciprocal theorem with a reciprocity gap J_R to account for nonlinear (elasto-plastic) deformation of the material

$$\int_{\partial R_1} \sigma_{ij} n_i \hat{u}_j dS + \int_{\partial R_2} \sigma_{ij} n_i \hat{u}_j dS = J_R + \int_{\partial R_1} \hat{\sigma}_{ij} n_i u_j dS + \int_{\partial R_2} \hat{\sigma}_{ij} n_i u_j dS \tag{6}$$

where n_i is the outward normal vector to the boundary $\partial R = \partial R_1 + \partial R_2$, and $\hat{S}[\hat{\sigma}_{ij}, \hat{u}_j]$ is the linear elastic fields of an auxiliary body with the same (E, v) as the elastic properties of the real body. We express the unknown cohesive tractions $t_i = \sigma_{ij} n_j$ along ∂R_1 as a Fourier series

$$t_i|_{\partial R_1} = \sum_{k=1}^{N} A_k^i \sin\frac{2k\pi x_1}{L} + \sum_{k=0}^{N} B_k^i \cos\frac{2k\pi x_1}{L} \tag{7}$$

where $L = 117D$ is the length of the domain encompassing the 117 Gurson cell elements, k is the wave number, and A_k^i and B_k^i are the Fourier coefficients to be determined.

We use the analytical auxiliary (virtual) field proposed in Chew [31] which has traction free boundary conditions ($\hat{\sigma}_{ij} n_i = 0$) and non-zero virtual displacements ($\hat{u}_j \neq 0$) along ∂R_1. Then, (6) reduces to

$$\int_{\partial R_1} t_i \hat{u}_i dS = J_R + \int_{\partial R_2} \left(\hat{\sigma}_{ij} n_i u_j - \sigma_{ij} n_i \hat{u}_j\right) dS \tag{8}$$

For a linear elastic material, $J_R = 0$, and we can solve for the unknown Fourier coefficients (A_k^i, B_k^i) by substituting (7) in (8) to obtain the cohesive tractions. For an elasto-plastic background material, however, $J_R \neq 0$ and has to be determined iteratively through a self-consistent procedure detailed in [31]. Once a converged cohesive traction $t_2(x_1)$ has been established ($t_1 \sim 0$ under K_I loading), we can then directly obtain the corresponding cohesive separations $\delta_2(x_1) = 2u_2(x_1)$. Note that this (t_2, δ_2) relationship is the equivalent crack-tip cohesive zone law representing the diffuse porous process zone in an elasto-plastic surrounding body, and does not include the contribution of background plastic dissipation. As schematically shown in Fig. 1c, the reconstructed cohesive zone law can be introduced in place of the process zone in an elasto-plastic medium to simulate the full transition from fracture initiation to steady-state toughness. Because this inverse method solution to reconstruct the crack-tip cohesive zone

law is sensitive to numerical errors, we implement a highly refined mesh along ∂R_2 to increase the resolution of the measured (σ_{ij}, u_j) as shown by the close-up view of the finite element mesh in Fig. 1d.

3. Results

3.1 Uniformly porous process zone

The diffuse fracture process zone (FPZ) consists of several rows of porous cell elements. This allows the crack to propagate freely within the FPZ, and is distinct from prior crack growth studies that simplify damage process modeling by confining crack growth to a narrow FPZ viz. a single row of porous cell elements ahead of the crack [32,34,35]. Figure 2a shows the fracture resistance curves $J/(\sigma_0 D)$ for crack advance $\Delta a/D$ within a diffuse versus narrow FPZ. Each cell element within the process zone has the same initial porosity of $f_0 = 0.005$ which resembles the void fractions for nucleated cavities in metals [32]. The initial crack growth within both process zones is characterized by a rapid increase in $J/(\sigma_0 D)$, but the diffuse FPZ exhibits a nearly two-fold higher steady-state fracture toughness J_{ss} at $\Delta a = 5D$; the J_{ss} steadily increases with Δa, indicating continued toughening in the presence of a diffuse FPZ. To validate our numerical calculations, we consider the mechanical properties of Mg ($E = 38$ to 120 GPa; $\sigma_0 =$ 21 to 460 MPa), which are similar to the parameters adopted in our simulation model. For the typical material parameters of $E = 50$ GPa, $v = 0.3$, $\sigma_0 = 200$ MPa, with $D = \sim 12$ μm (order of the maximum particulate size) for Mg alloy, the fracture toughness $J = 2\sigma_0 D$ to $3\sigma_0 D$ for crack growth within the diffuse FPZ in Fig. 2a translates to 4.8-7.2 kJ/m^2 which is close to the reported fracture toughness of 5.6-7.8 kJ/m^2 for Mg alloy [49].

To provide a complete picture of the fracture process within the narrow and diffuse FPZ, we compare in Fig. 2b and 2c the evolution of the sequence of voiding f and mean stress σ_m/σ_0 along $x_2/D = 0$, at $\Delta a = 20, 40$ and $60D$. Observe that the porosity evolution for both the narrow and diffuse process zones are almost identical, since the crack in both FPZs grows symmetrically along the initial crack path by a void-by-void mechanism. High stress concentrations at the crack-tip, corresponding to the peak σ_m, drives the rapid increase in f to reach $f_c = 0.2$ where the cell element is rendered extinct. The rapid and sequential voiding result in significant stress relaxation, and shift the peak σ_m forward, thus advancing the crack. Interestingly, the post-peak σ_m distributions are consistently higher with a diffuse FPZ, which is indicative of a larger damage extent ahead of the crack and contributes to the two-fold higher J_{ss} in Fig. 2a.

Figure 3a and 3b shows the converged traction t_2/σ_0 and separation δ_2/D distributions along $x_2/D = 0$ of the diffuse FPZ. These reconstructed traction and separation distributions (solid lines) from nonlinear FPM, as outlined in Section 2.2, are in relatively good agreement with those from direct FEM calculations taken along the crack front (symbols). Figure 3c shows the corresponding traction-separation relationship, constituting the crack-tip cohesive zone law. At $\Delta a = 10D$, the field-projected t_2 tractions are non-zero behind the crack at $x_1/D = 0$, because of the periodic boundary assumption of the Fourier series in (7); this boundary error diminishes with crack length. Convergence of the cohesive zone law by nonlinear FPM is achieved at $\Delta a = 20D$, and a similar (t_2, δ_2) relationship is obtained at $\Delta a = 55D$.

3.2 Two-scale porosity effects on micromechanics of cracking

The diffuse FPZ with uniform porosity of $f_0 = 0.005$ provides a baseline understanding of crack growth in a homogeneous material relatively free of larger-scale defects, such as metals

and alloys produced by traditional manufacturing processes. In the following, we introduce an inhomogeneous distribution of larger-scale defects, as quantified by two parameters: β denoting the porosity of the larger-scale voids relative to a background porosity of $f_0 = 0.005$, and α denoting the percentage proportion of these larger-scale voids in the diffuse FPZ. Here, we consider the range of α from 0.5 to 10 and β from 1 to 10, with the higher spectrum resembling larger-scale defects formed by unsintered powder in additively-manufactured metals. Because the contributions of the larger-scale voids to the fracture behavior will be highly statistical, we will use the same random seed in our implementation, such that the location of larger-scale voids in an FPZ with high α will encompass that in an FPZ with a smaller α. Figure 4 displays the effects of α and β on the fracture resistance curves. Observe that larger-scale voids with $\beta = 1.5$ do not significantly change $J/(\sigma_0 D)$, even at high percentage proportions of $\alpha = 10$. Increasing the porosity of the larger-scale void to $f_0 = 0.025$ or 0.05, represented by $\beta = 5$ or 10, however, significantly decreases the fracture toughness across all $\alpha > 1$. These results suggest that the mere presence of larger size-scale defects will significantly reduce the overall fracture toughness, provided these defects are considerably larger than the background porosity such as in additively-manufactured metals [11-16].

Figure 5 depicts the porosity distributions and fracture paths for the diffuse process zones with varying α and β. For each (α,β) pair, we include contours of the porosity distributions at three different $\Delta a/D$ to illustrate the cracking sequence. At $\beta = 1.5$, the crack remains straight with voiding confined to a narrow damage zone ahead of the crack. At $\beta = 5$, the crack path is now influenced by the presence of the larger-scale voids. While the crack remains relatively straight when there are few larger voids at $\alpha = 1$, we start to see the effects of the larger-scale voids in controlling the crack path at $\alpha = 3$ and 5. Unconnected voiding regions nucleating from

larger-scale voids near the crack-tip now result in the formation of multiple damage zones, which eventually link up with the main crack. At $\alpha = 10$, the proportion of larger-scale voids is now sufficient to allow multiple cracks initiating from high porosity regimes in the FPZ to grow somewhat independently, before coalescing with the main crack. This mechanism becomes dominant across all α values at $\beta = 10$, where multiple unconnected damage zones are formed to cause significant undulations in the crack path.

Because of the undulating crack paths for varying (α, β), the traction distributions cannot be directly ascertained from finite element measurements of σ_{22} distributions along $x_2 = 0$. Instead, the nonlinear FPM effectively homogenizes the damage within the diffuse FPZ to an equivalent traction distribution in a crack-tip cohesive zone binding two elasto-plastic materials together. Figure 6 shows the reconstructed t_2 tractions, taken at $\Delta a/D = 25$, at which point the cohesive zone becomes fully developed (i.e. cohesive tractions drop to zero along x_1/D). Direct measurements of the t_2 tractions (symbols) along $x_2 = 0$ by FEM are in good agreement with the reconstructed tractions from nonlinear FPM in the post-peak regime ($\Delta a/D > 25$). However, these tractions by FEM display significant fluctuations within the cohesive zone ($\Delta a/D < 25$), which are effectively averaged out by nonlinear FPM.

We show in Fig. 7 the equivalent crack-tip cohesive zone laws by nonlinear FPM for diffuse process zones with varying (α, β). Results consistently show that the peak tractions, which reside close to the current crack-tip ($f_{tip} = 0.1$), are reached during early separation. The extracted cohesive zone law for the dual size-scale porous process zone therefore resembles a linear or slightly concaving traction-separation law. Observe that increasing α and/or β generally decreases the cohesive energy, by reducing both the peak traction as well as the critical separation δ_0 in Fig. 1c. At $\beta = 1.5$, the 50% higher porosity of the larger-scale voids do not

significantly change the peak traction across all α. The effects of α become more pronounced for $\beta = 5$: the peak traction decreases from $3.1\sigma_0$ to $2.6\sigma_0$ as α increases from 1 to 3 but saturates thereafter, while δ_0 proportionally decreases with increase in α. When the variation in void porosity becomes an order of magnitude higher at $\beta = 10$, the traction-separation relationship does not significantly change beyond $\alpha = 3$, which suggests saturation in the effects of the larger-scale voids on the cracking behavior. We remark that the initial drop in peak cohesive tractions with increase in α for $\beta = 5$ and 10 (Fig. 7b and 7c) leads to significant reduction in the corresponding steady-state fracture toughness (Fig. 4b and 4c). This trend is in agreement with studies by Hutchinson and Evans [50] which show that small changes to the peak cohesive strength with values of $\sim 3\sigma_0$ can cause dramatic changes to the steady-state fracture toughness.

3.3 Two-scale porosity effects on statistical fracture toughness

Because the fracture toughness maybe sensitive to the exact location of the larger-scale voids with respect to the growing crack, we perform 10 independent simulation runs with different random seeds for each (α, β) pair. The symbols in Fig. 8a as well as the contour plot in Fig. 8b denote the average steady-state fracture toughness J_{ss} values from these runs, as a function of (α, β). We also show as error bars in Fig. 8a as well as the contour plot in Fig. 8c the standard errors in J_{ss} associated with these simulation runs. Unsurprisingly, the FPZ with $\beta = 1.5$, which is close to being uniformly porous, has the highest average J_{ss}. However, increasing α for such a process zone can in fact increase the toughness, which is counterintuitive and clearly relates to the location of the larger-scale void with respect to the crack path. The presence of a larger-scale void directly ahead of the crack, for example, would accelerate the void coalescence process with the crack-tip and lower J_{ss}, while the larger-scale voids in the vicinity of, but not along, the initial crack path can instead cause deviations in the crack paths to increase J_{ss}. Increasing β

generally lowers J_{ss}, though the effects become negligible beyond $\beta > 5$, as seen by the similar average J_{ss} values for $\beta = 5$ and 10 with the same α. For $\beta \geq 2$, the initial increase in α from 1 to 4 significantly decreases J_{ss}, but J_{ss} remains unchanged beyond this point. These results suggest a limiting effect of the size (β) and number (α) of larger-scale voids on the fracture toughness.

There are a number of exceptions to the general trends in the relationship between J_{ss} and (α, β) detailed above, specifically at $\alpha = \beta = 3$ where a higher than expected J_{ss} comparable to $\alpha = 3, \beta = 2$ is obtained. Close examination of the statistical fluctuations in J_{ss} also show unusually high standard errors at $\alpha = \beta = 3$ (Fig. 8c), indicating that the fracture resistance is highly sensitive to the location of the larger-scale voids with respect to the growing crack. Higher than expected J_{ss} is also seen at $\alpha = 2, \beta = 8$, though not at the same extent as $\alpha = \beta = 3$. To understand the statistical effects, we show in Fig. 9a the fracture resistance curves for all 10 independent simulation runs with $\alpha = \beta = 3$. Observe that the fracture resistance spans several-folds: $1 \leq J/(\sigma_0 D) \leq 4$. Figure 9b and 9c shows the cracking progression and porosity distribution for the FPZ with the maximum (seed 5) and minimum fracture toughness (seed 6). The toughening mechanism for the former (seed 5) is solely attributed to the unique distribution of these larger-scale voids. During initial crack growth ($\Delta a/D = 5$), one of the larger-scale voids strategically located at ~60º below the crack-tip is caught within the active plastic zone and grows rapidly. This cavitation process dissipates significant amount of energy, and shields the crack-tip. The reduced stress concentration at the crack-tip leads to a continuously increasing fracture resistance up to $\Delta a/D = 8$. At this juncture, the crack-tip shielding allows high hydrostatic stresses (σ_m) to develop further ahead of the crack, which triggers the cavitation of two larger-scale voids in the vicinity to form multiple damage zones akin to that for a

constrained ductile film [33,36,37]. These larger-scale voids grow and coalesce with the neighboring background voids to form a new micro-crack at $\Delta a/D = 23$ which is unconnected to the main crack. The interaction between the micro-crack and the main crack in turn causes ligament thinning and eventual coalescence. In contrast, the low toughness FPZ (seed 6) has a cluster of 4 large voids located within $\sim 7D$ of the initial crack-tip. Rapid growth and coalescence of these voids with the crack-tip leads to rapid propagation of the crack at low $J/(\sigma_0 D)$ to form a contiguous damage zone. Statistically, seed 5 constitutes a rare event, since majority of the J_{ss} values in Fig. 9a for our simulation runs (including seed 6) fluctuate around $1.5\sigma_0 D$.

4. Discussions and Conclusion

The interaction between dual size-scale voids and the effects on the crack path and overall fracture resistance have significant implications for additively-manufactured (AM) metals processed through direct metal laser sintering (DMLS). This 3D printing technique uses lasers to selectively melt ultra-thin layers of deposited metallic powder in a layer-by-layer fashion, until the build is complete [51]. Such AM metals by DMLS can contain a distribution of void sizes, ~20-40 μm in diameter [52], which are either gas entrapment voids or voids originating from unsintered powder particles [11-16]. These larger-scale voids are in addition to the smaller-scale background porosity seen on postmortem fracture surfaces of both AM and conventional metals. The background porosity typically originates from nucleated cavities of reinforcement particulates, such as MnS particles in steel which have diameters ranging from ~2-12 μm [53].

While the uniaxial strength properties of AM metals are comparable to conventional metals of the same type [15], the fracture and fatigue response behavior are highly statistical. In a batch of AM Ti6Al4V samples produced under the same processing conditions, for example, certain

number of these samples exhibited good fatigue life, while others experienced catastrophic failure during early load cycling [52]. The fracture surfaces of these groups of samples reveal similar level of larger-scale void porosity, though the presence of clusters of larger-scale voids close to the initial crack-front was suspected to be the reason for the premature failure [52]. Our results appear to support this experimental observation. In a real material, the distance from the crack tip to the larger-scale voids will vary from one position to another along the crack front, but the parameter of importance is the average location of these voids relative to the crack front. Accordingly, the porosities in our 2D analysis represent the average through-thickness porosities in that of a real sample. The smaller-scale voids are uniformly distributed within the sample, and have the same average background porosity. The larger-scale voids, however, are more sparsely distributed and the locations of these larger-scale voids in our 2D analysis represent the mean positions with porosities that are averaged through the thickness. While increasing the size (β) and quantity (α) of these larger-scale voids relative to the smaller-scale background porosity generally decreases the fracture toughness, the effects of (β, α) can be diminished in some instances or even reversed in other instances to increase the fracture toughness. This is apparent for FPZs with $\alpha = \beta = 3$ where unusually high average fracture toughness values, along with large statistical variations in toughness, are observed (Fig. 8a and 9a). The presence of a cluster of larger-scale voids in the vicinity of the initial crack-tip, in particular, facilitates the void link up process and results in low toughness (Fig. 9c). However, the presence of larger-scale voids within the active plastic zone of the crack-tip can shield the crack-tip and induce the development of multiple damage zones nucleating at larger-scale voids some distances from the crack-tip (Fig. 9b). Our results show that such damage mechanisms can improve fracture toughness by four-folds.

The measured fracture toughness $J/(\sigma_0 D)$ for mode I crack growth within the various FPZs have combined contributions from background plasticity, as well as void growth and coalescence mechanisms operative within the porous FPZs. We delineate these contributions through a nonlinear FPM [31] to reconstruct an equivalent crack-tip cohesive zone law operating within an elasto-plastic background material, as schematically shown in Fig. 1c. The micromechanical void growth and coalescence mechanics operative within the diffuse FPZ are homogenized as a cohesive zone traction-separation law, and the resulting cohesive energy Γ_0 is the associated fracture toughness contribution; $J_{ss} - \Gamma_0$ can thus be delineated as the approximate contribution from background plasticity [32]. We find that Γ_0/J_{ss} for the cohesive zone laws in Fig. 7 generally ranges from 0.4-0.6 for the various (β, α) parameters, suggesting almost equal contributions from both background plasticity and crack-growth micromechanics within the process zone. Interestingly, this extracted value of Γ_0 from field projection is consistently several-folds higher than the fracture initiation toughness value of $J/(\sigma_0 D) = \sim 0.3$ across the various (β, α) parameters in Fig. 4. This discrepancy arises because the extraction of the cohesive zone law from field projection is conducted during steady-state cracking; the stress fields associated with this crack propagation phase is clearly different from those associated with cracking initiation conditions, which modifies the rate of growth and coalescence of damage. This discrepancy in Γ_0 suggests that some evolution of the cohesive parameters from crack initiation to propagation should ideally be considered to account for this stress state evolution [54].

The ductile fracture of a conventional metal can be modeled with a uniformly porous FPZ, i.e. $\alpha = \beta = 1$, since the pores nucleate only from a single size-scale of inclusions or particulates; the fracture process can thus be described by a single cohesive zone law. In AM

metals, however, our results demonstrate that the fracture process is highly-sensitive to the relative size, proportion, and location of larger-scale voids statistically distributed within the diffuse process zone. As a result, the cohesive strength, cohesive energy, as well as functional form of the cohesive zone law, are strongly dependent on the dual void size-scales, which introduces a size-effect into the homogenized traction-separation relationship. Thus, AM metals of the same type may have different cohesive zone laws, as shown in Fig. 7, depending on the relative size of the larger-scale voids and the specifics of how these larger-scale voids are distributed.

We remark that the nonlinear FPM adopted in this paper [31] provides a bridge between detailed micromechanical damage modeling with Gurson cell elements and the crack-tip cohesive zone law. While modeling the process zone with Gurson cells provides detailed and realistic insights into the effects of the larger-scale voids on crack deflection and advancement, use of the Gurson cell introduces a physical length-scale parameter D representing the spacing between voids. This results in a potential scaling issue, since the minimum mesh size in the finite element model will be dictated by D. In contrast, no such scaling issues exists for the reconstructed crack-tip cohesive zone law by nonlinear FPM, which is suitable for large-scale computations [54] since it accounts for the dissipative mechanisms in a homogenized fashion (i.e. effects of D, f_0, etc. are smeared out).

In summary, we show that the presence of a population of voids considerably larger than the background porosity associated with conventional ductile fracture process can significantly affect the fracture toughness, crack paths, as well as the crack-tip cohesive zone laws. These findings have significant implications for AM metals where larger-scale voids are present. While increasing the size and number fractions of these larger-scale voids tend to lower the fracture

resistance, the results are highly statistical and depend on the exact location of these voids with respect to the crack-tip. In particular, we demonstrate that strategic placement of larger-scale voids within the active plastic zone can induce crack-tip shielding and trigger the formation of multiple, unconnected damage zones, both of which contribute to a four-fold increase in toughness.

Acknowledgements

The authors acknowledge the support of the National Science Foundation Grants Nos. NSF-DMR-18-09696 (Y.C. & H.B.C) and NSF-DMR-18-09640 (Y.F.G.).

References

[1] Gladysz, G.M., Chawla, K.K., 2014. Voids in Materials: From unavoidable defects to designed cellular materials, first ed. Elsevier, ISBN: 978-0-444-56367-5.
[2] Harpale, A., Sawant, S., Kumar, R., Levin, D., Chew, H.B., 2018. Ablative thermal protection systems: Pyrolysis modeling by scale-bridging molecular dynamics. Carbon 130, 315-324.
[3] Van Stone, R.H., Cox, T.B., Low Jr., J.R., Psioda, J.A., 1985. Microstructural aspects of fracture by dimpled rupture. Int. Met. Rev. 30, 157-179.
[4] Faleskog, J., Shih, C.F., 1997. Micromechanics of coalescence – I. Synergistic effects of elasticity, plastic yielding and multi-size scale voids. J. Mech. Phys. Solids 45, 21-50.
[5] Chew, H.B., Guo, T.F., Cheng, L., 2006. Effects of pressure-sensitivity and plastic dilatancy on void growth and interaction. Int. J. Solids Struct. 43, 6380-6397.
[6] Tvergaard, V., 1998. Interaction of very small voids with larger voids. Int. J. Solids Struct. 35, 3989-4000.
[7] Perrin, G., Leblond, J.-B., 2000. Accelerated void growth in porous ductile solids containing two populations of cavities. Int. J. Plasticity 16, 91-120.
[8] Tvergaard, V., 1996. Effect of void size difference on growth and cavitation instabilities. J. Mech. Phys. Solids 44, 1237-1253.
[9] Tekoglu, C., 2015. Void coalescence in ductile solids containing two populations of voids. Eng. Fract. Mech. 147, 418-430.
[10] Tekoglu, C., Nielsen, K.L., 2019. Effect of damage-related microstructural parameters on plate tearing at steady state. Europ. J. Mech. A Solids 77, 103818.
[11] Sterling, A., Shamsaei, N., Torries, B., Thompson, S.M., 2015. Fatigue behavior of additively manufactured Ti-6Al-4V. Procedia Eng. 133, 576-589.
[12] Tammas-Williams, S., Withers, P., Todd, I., Prangnell, P., 2017. The influence of porosity on fatigue crack initiation in additively manufactured titanium components. Sci. Rep. 7, 7308.
[13] Galarraga, H., Lados, D.A., Dehoff, R.R., Kirka, M.M., Nandwana, P., 2016. Effects of the microstructure and porosity on properties of Ti-6Al-4V ELI alloy fabricated by electron beam melting (EBM). Addit. Manuf. 10, 47-57.

[14] Edwards, P., O'Connor, A., Ramulu, M., 2013. Electron beam additive manufacturing of titanium components: Properties and performance. J. Manuf. Sci. Eng. 135, 061016.
[15] Foehring, D., Chew, H.B., Lambros, J., 2018. Characterizing the tensile behavior of additively manufactured Ti-6Al-4V using multiscale digital image correlation. Mater. Sci. Eng. A 724, 536-546.
[16] Liu, S., Shin, Y.C., 2019. Additive manufacturing of Ti6Al4V alloy: A review. Materials & Design 164, 107552.
[17] Dugdale, D.S., 1960. Yielding of steel sheets containing slits. J. Mech. Phys. Solids 8, 100-108.
[18] Barenblatt, G.I., 1962. The mathematical theory of equilibrium cracks in brittle fracture. Adv. Appl. Mech. 7, 55-129.
[19] Guo, Z.K., Kobayashi, A.S., Hay, J.C., White, K.W., 1999. Fracture process zone modeling of monolithic Al_2O_3. Eng. Fract. Mech. 63, 115-129.
[20] Williams, J.G., Hadavinia, H., 2002. Analytical solutions for cohesive zone models. J. Mech. Phys. Solids 50, 809-825.
[21] Valoroso, N., Fedele, R., 2010. Characterization of a cohesive-zone model describing damage and de-cohesion at bonded interfaces. Sensitivity analysis and mode-I parameter identification. Int. J. Solids Struct. 47, 1666-1677.
[22] Tvergaard, V., Hutchinson, J.W., 1992. The relation between crack growth resistance and fracture process parameters in elastic-plastic solids. J. Mech. Phys. Solids 40, 1377-1397.
[23] Chandra, N., Li, H., Shet, C., Ghonem, H., 2002. Some issues in the application of cohesive zone models for metal–ceramic interfaces. Int. J. Solids Struct. 39, 2827-2855.
[24] Li, K., Chandra, N., 2003. Analysis of crack growth and crack-tip plasticity in ductile materials using cohesive zone models. Int. J. Plast. 19, 849-882.
[25] Murphy, N., Ivankovic, A., 2005. The prediction of dynamic fracture evolution in PMMA using a cohesive zone model. Eng. Fract. Mech. 72, 861-875.
[26] Olden, V., Thaulow, C., Johnsen, R., Østby, E., Berstad, T., 2008. Application of hydrogen influenced cohesive laws in the prediction of hydrogen induced stress cracking in 25%Cr duplex stainless steel. Eng. Fract. Mech. 75, 2333-2351.
[27] Hong, S., Chew, H.B., Kim, K.-S., 2009. Cohesive-zone laws for void growth – I. Experimental field projection of crack-tip crazing in glassy polymers. J. Mech. Phys. Solids 57, 1357-1373.
[28] Chew, H.B., Hong, S., Kim, K.-S., 2009. Cohesive zone laws for void growth – II. Numerical field projection of elasto-plastic fracture processes with vapor pressure. J. Mech. Phys. Solids 57, 1374-1390.
[29] Kim, H.G., Chew, H.B., Kim, K.-S., 2012. Inverse extraction of cohesive zone laws by field projection method using numerical auxiliary fields. Int. J. Numer. Meth. Eng. 91, 516-530.
[30] Chew, H.B., 2014. Cohesive zone laws for fatigue crack growth: Numerical field projection of the micromechanical damage process in an elasto-plastic medium. Int. J. Solids Struct. 51, 1410-1420.
[31] Chew, H.B., 2013. Inverse extraction of interfacial tractions from elastic and elasto-plastic far-fields by nonlinear field projection. J. Mech. Phys. Solids 61, 131-144.
[32] Xia, L., Shih, C.F., 1995. Ductile crack growth – I. A numerical study using computational cells with microstructurally-based length scales. J. Mech. Phys. Solids 43, 233-259.

[33] Chew, H.B., Guo, T.F., Cheng, L., 2005. Vapor pressure and residual stress effects on failure of an adhesive film. Int. J. Solids Struct. 42, 4795-4810.
[34] Chew, H.B., Guo, T.F., Cheng, L., 2004. Vapor pressure and residual stress effects on the toughness of polymeric adhesive joints. Eng. Fract. Mech. 71, 2435-2448.
[35] Chew, H.B., Guo, T.F., Cheng, L., 2005. Vapor pressure and residual stress effects on mixed mode toughness of an adhesive film. Int. J. Fract. 134, 349-368.
[36] Chew, H.B., Guo, T.F., Cheng, L., 2007. Pressure-sensitive ductile layers–I. Modeling the growth of extensive damage. Int. J. Solids Struct. 44, 2553-2570.
[37] Chew, H.B., Guo, T.F., Cheng, L., 2007. Pressure-sensitive ductile layers–II. 3D models of extensive damage. Int. J. Solids Struct. 44, 5349-5368.
[38] Pardoen, T., Hutchinson, J.W., 2003. Micromechanics-based model for trends in toughness of ductile metals. Acta Mater. 51, 133-148.
[39] Gurson, A.L., 1977. Continuum theory of ductile rupture by void nucleation and growth: Part I – Yield criteria and flow rules for porous ductile media. Trans. J. Eng. Mater. Tech. 99, 2-15.
[40] Tvergaard, V., 1990. Material failure by void growth to coalescence. Adv. Appl. Mech. 27, 83-151.
[41] Faleskog, J., Gao, X., Shih, C.F., 1998. Cell model for non-linear fracture analysis – I. Micromechanics calibration. Int. J. Fract. 89, 355-373.
[42] Xia, L., Shih, C.F., 1995. Ductile crack growth – II. Void nucleation and geometry effects on macroscopic fracture behavior. J. Mech. Phys. Solids 43, 1953-1987.
[43] Moran, B., Shih, C.F., 1987. A general treatment of crack tip contour integrals. Int. J. Fract. 35, 363-371.
[44] Hong, S., Kim, K.-S., 2003. Extraction of cohesive-zone laws from elastic far-fields of a cohesive crack tip: a field projection method. J. Mech. Phys. Solids 51, 1267-1286.
[45] Li, R., Chew, H.B., 2017. Grain boundary traction signatures: Quantifying the asymmetrical dislocation emission processes under tension and compression. J. Mech. Phys. Solids 103, 142-154.
[46] Li, R., Chew, H.B., 2016. Grain boundary traction signatures: Quantitative predictors of dislocation emission. Phys. Rev. Lett. 117, 085502.
[47] Mohan, S., Li., R. Chew, H.B., 2018. Local stress analysis of partial dislocation interactions with symmetrical-tilt grain boundaries containing E-structural units. Phil. Mag. 25, 2345-2366.
[48] Cui. Y., Chew, H.B., 2019. A simple numerical approach for reconstructing the atomic stresses at grain boundaries from quantum-mechanical calculations. J. Chem. Phys. 150, 144702.
[49] Somekawa, H., Mukai, T., 2006. Fracture toughness in a rolled AZ31 magnesium alloy. J. Alloys Compd. 417, 209-213.
[50] Hutchinson, J.W., Evans, A.G., 2000. Mechanics of materials: Top-down approaches to fracture. Acta Mater. 48, 125-135.
[51] Lewandowski, J.J., Seifi, M., 2016. Metal additive manufacturing: A review of mechanical properties. Annu. Rev. Mater. Res. 46, 151-186.
[52] Vansickle, R., 2019. Microscale strain accumulation during fatigue and fracture of additively-manufactured Ti-6Al-4V. Mater of Science Thesis, University of Illinois at Urbana-Champaign.

[53] Zhang, X., Zhang, L., Yang, W., Dong, Y., 2017. Characterization of MnS particles in heavy rail steels using different methods. Steel Res. Int. 88, 1600080.
[54] Nielsen, K.L., Hutchinson, J.W., 2012. Cohesive traction-separation laws for tearing of ductile metal plates. Int. J. Impact Eng. 48, 15-23.

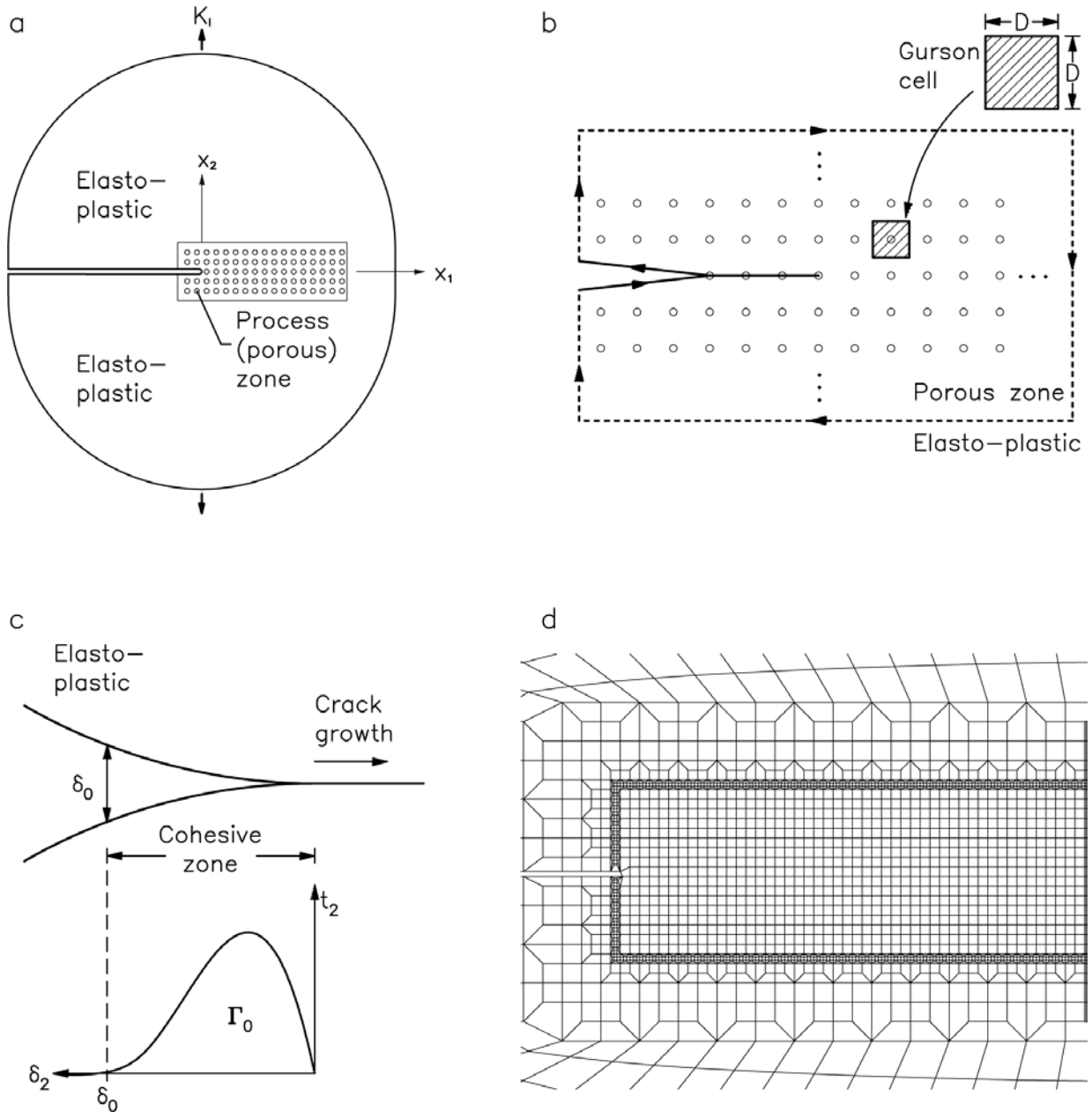

Figure 1: (**a**) Schematic of a small-scale yielding model with a porous process zone embedded within an elasto-plastic background material. (**b,c**) Porous process zone represented by several rows of void-containing Gurson cell elements (**b**); dashed lines denote the integration domain for field projection of the equivalent crack-tip cohesive tractions in a non-porous elasto-plastic medium for construction of the crack-tip cohesive zone laws (**c**). (**d**) Close-up view of the finite element mesh, with refined mesh along the integration domain for nonlinear field projection.

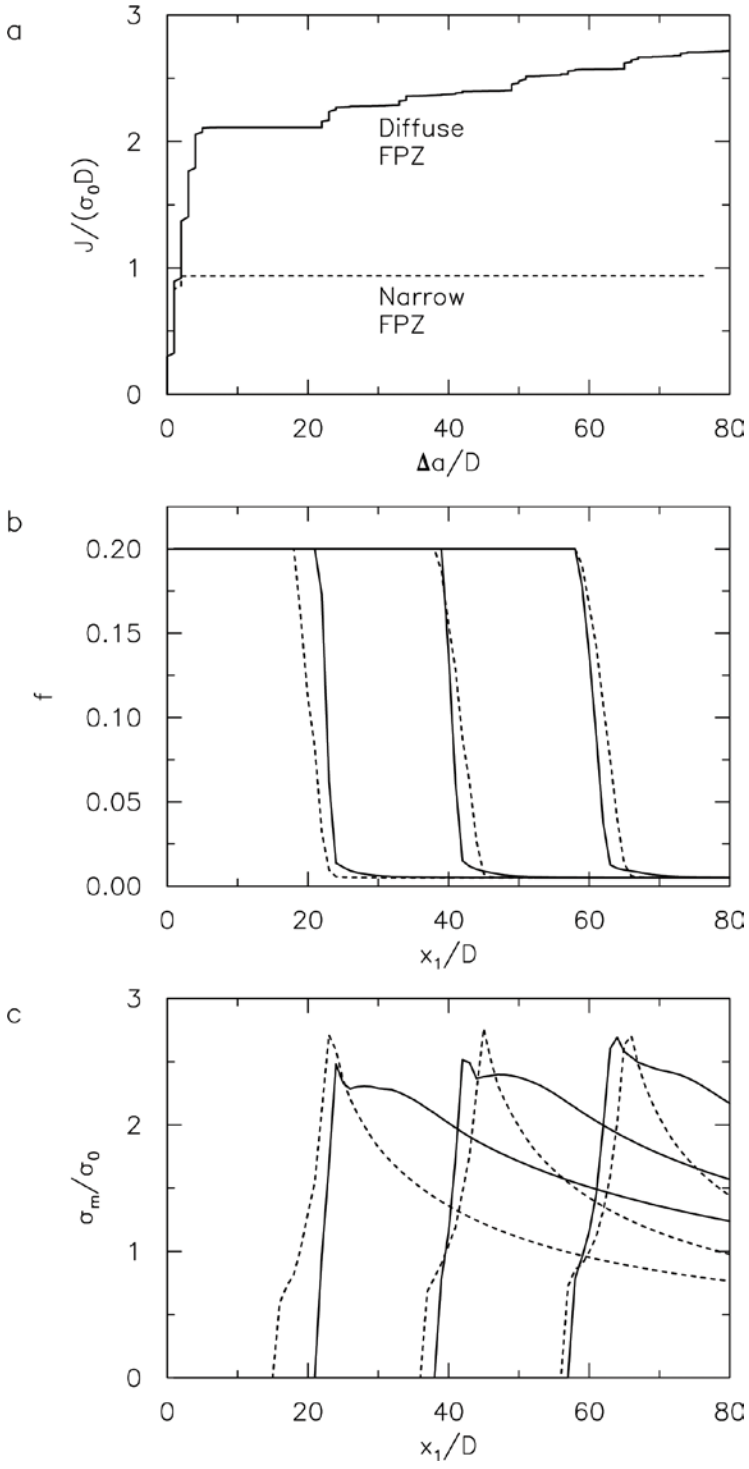

Figure 2: (**a**) Crack growth resistance curves, as well as (**b**) porosity and (**c**) mean stress distributions along $x_2 = 0$ for crack growth within a diffuse (solid lines) and narrow (dashed lines) fracture process zone (FPZ) with uniform porosity.

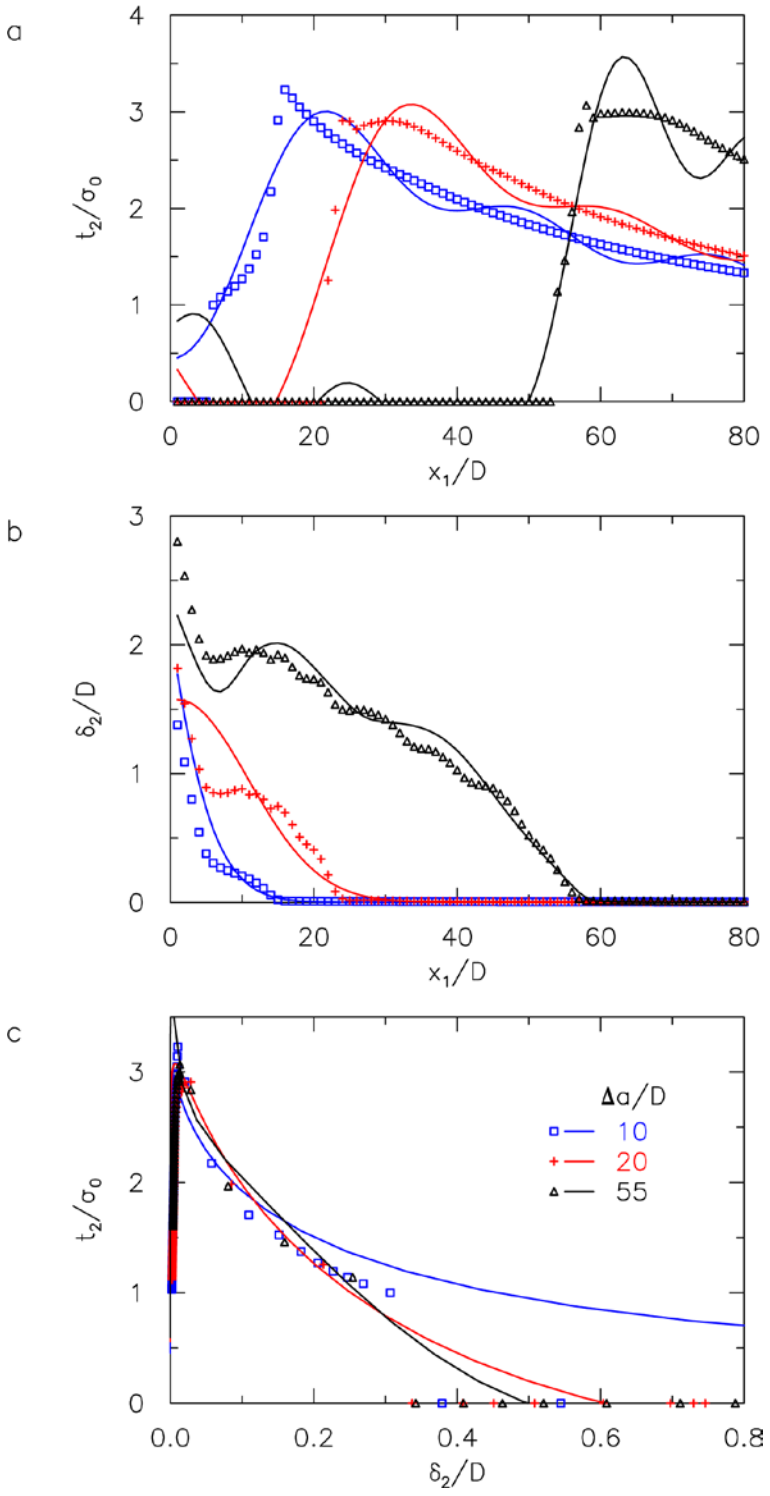

Figure 3: Equivalent traction (**a**) and separation (**b**) distributions along $x_2 = 0$ and corresponding cohesive zone laws (**c**) for crack growth within a diffuse FPZ with uniform porosity. Solid lines are from nonlinear field projection; symbols are from finite element calculations.

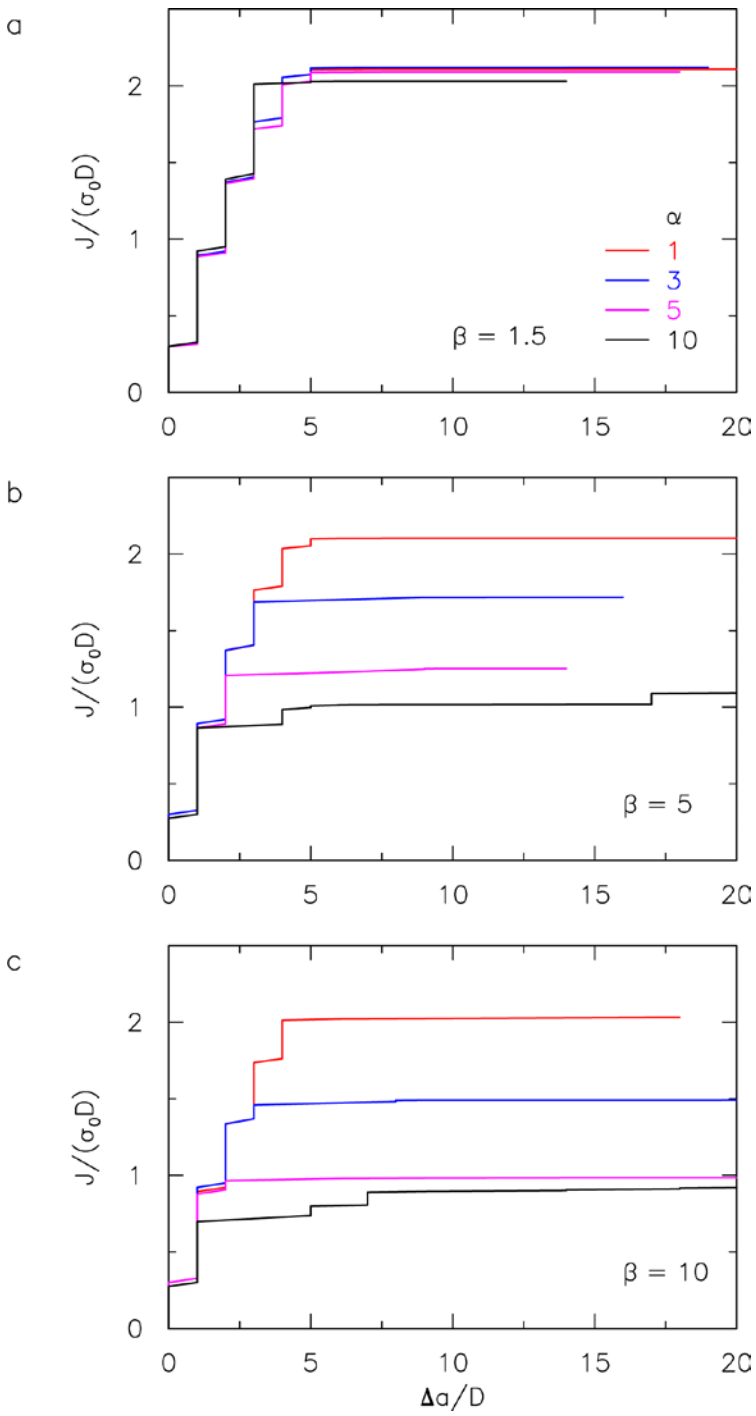

Figure 4: Fracture resistance curves for crack growth within diffuse FPZs containing two size-scales of voids; β and α denote the relative porosity and percentage proportion of the larger-scale voids.

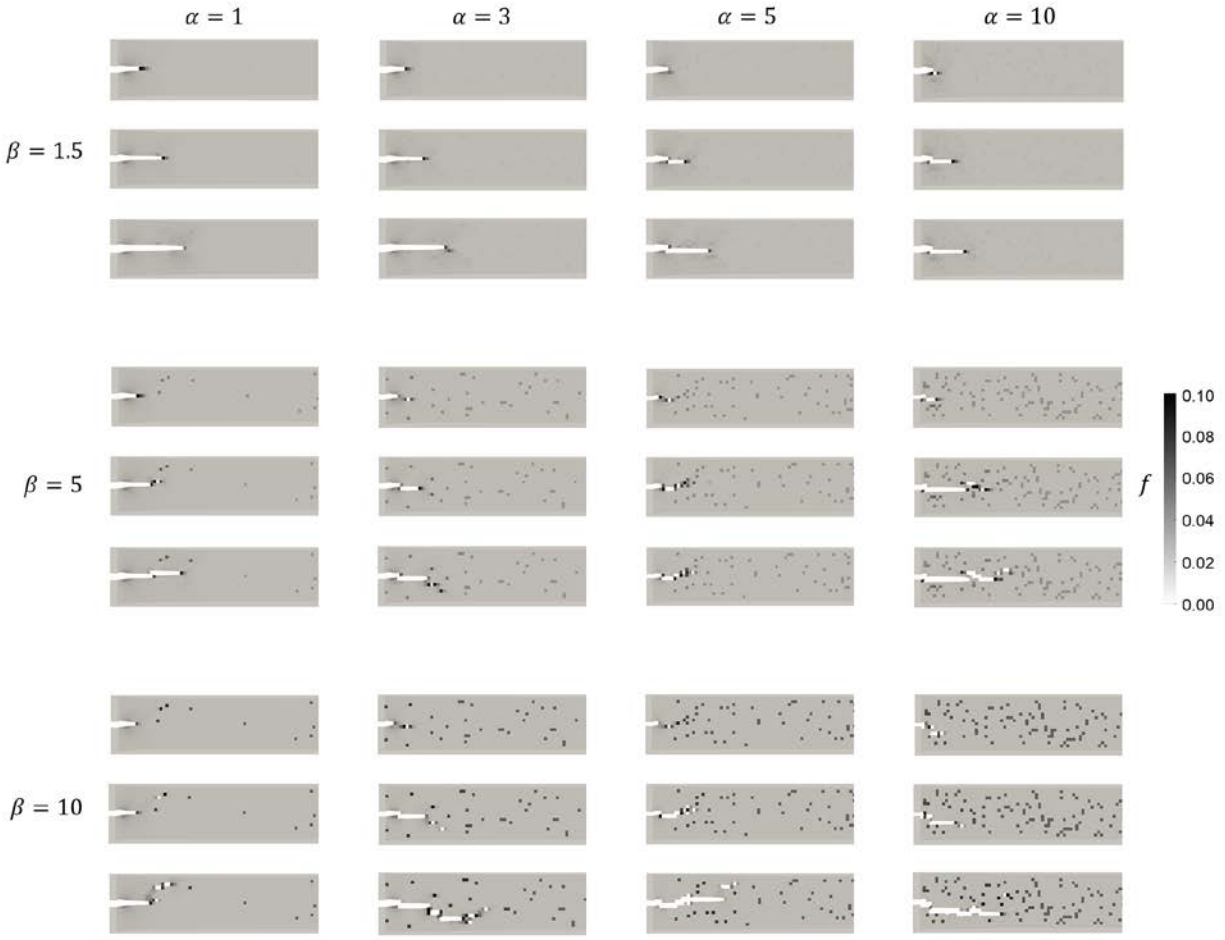

Figure 5: Crack growth profiles within diffuse FPZs containing two size-scales of voids; β and α denote the relative porosity and percentage proportion of the larger-scale voids.

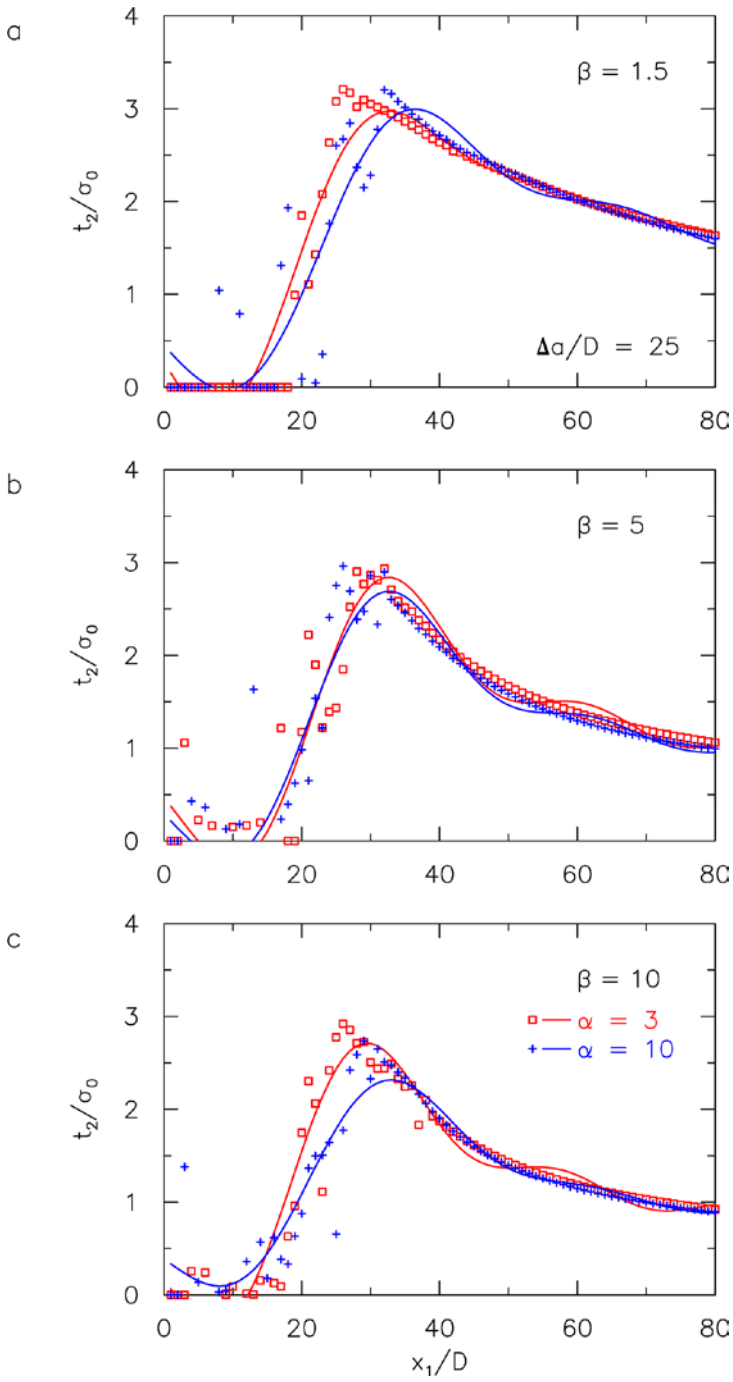

Figure 6: Equivalent traction distributions along $x_2 = 0$ for crack growth within diffuse FPZs containing two size-scales of voids; β and α denote the relative porosity and percentage proportion of the larger-scale voids. Solid lines are from nonlinear field projection; symbols are from finite element calculations.

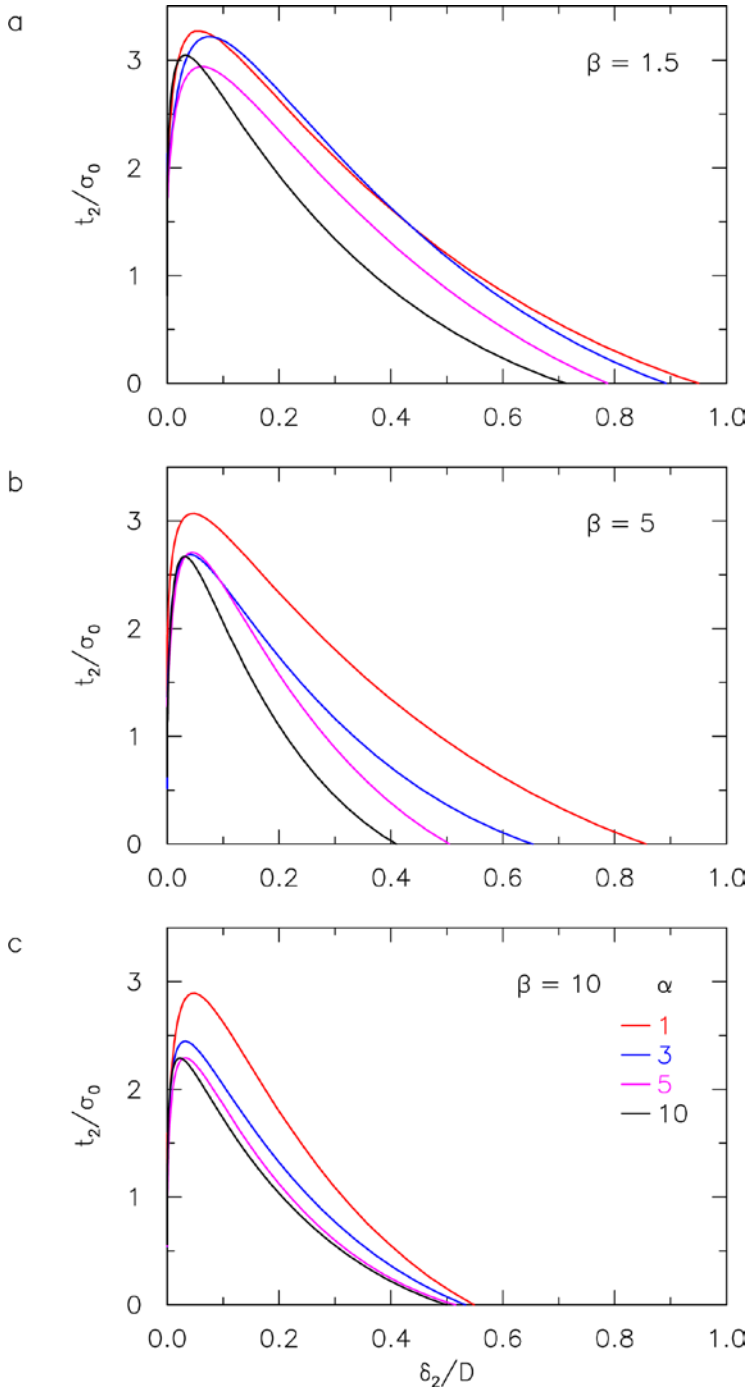

Figure 7: Equivalent cohesive zone laws for crack growth within diffuse FPZs containing two size-scales of voids; β and α denote the relative porosity and percentage proportion of the larger-scale voids.

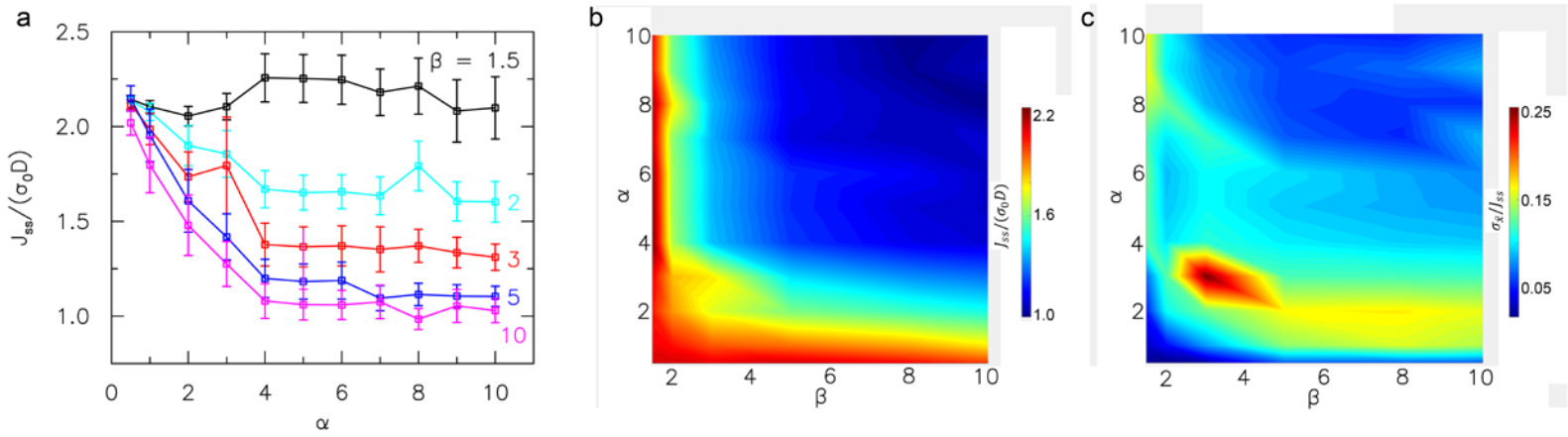

Figure 8: (**a**) Average steady-state fracture toughness $J_{ss}/(\sigma_0 D)$ for crack growth within diffuse FPZs containing two size-scales of voids; β and α denote the relative porosity and percentage proportion of the larger-scale voids. Error bars denote the standard error over 10 simulation runs with different random seeds. (**b,c**) Contours of $J_{ss}/(\sigma_0 D)$ and corresponding standard error as a function of (β, α).

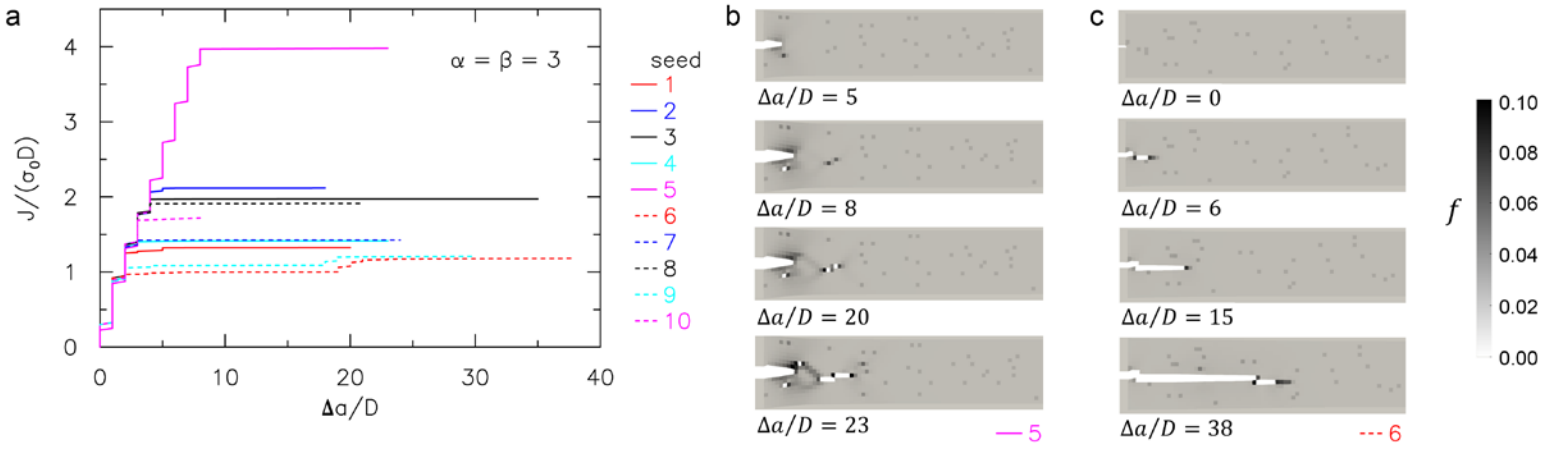

Figure 9: Statistical variations in the fracture resistance curves (**a**) and evolutions in crack profiles (**b,c**) for crack-growth within diffuse FPZs containing two size-scales of voids; the 10 random samples have the same relative porosity ($\beta = 3$) and percentage proportion ($\alpha = 3$) of larger-scale voids.